Carbon Allotrope Nanomaterials Based Catalytic Micromotors

R. Maria-Hormigos,[†] B. Jurado-Sanchez,[*,†] L. Vazquez,[§] and A. Escarpa[*,†]

[†]Department of Analytical Chemistry, Physical Chemistry, and Chemical Engineering, University of Alcala, Alcala de Henares, E-28871 Madrid, Spain

[§]Institute of Materials Science of Madrid (ICMM-CSIC), Cantoblanco, E-28049 Madrid, Spain

ABSTRACT: *Carbon allotropes nanomaterials are explored here for the preparation of highly efficient tubular micromotors: 0D (C60 fullerene), 1D (carbon nanotubes), 2D (graphene), and 3D (carbon black, CB). The micromotors are prepared by direct electrochemical reduction or deposition of the nanomaterial into the pores of a membrane template. Subsequent electrodeposition of diverse inner catalytic layers (Pt, Pd, Ag, Au, or MnO_2) allows for efficient bubble-propulsion in different media (seawater, human serum, and juice samples). Atomic-force microscopy (AFM) and scanning electron microscopy characterization reveals that the micromotors exhibit a highly rough outer surface and highly microporous inner catalytic structures. A key aspect derived from the AFM characterization is the demonstration that the rough outer surface of the micromotors can greatly affect their overall speed. To date, the literature has only focused on studying the effect of the inner catalytic layer upon their speed and performance and has underestimated the effect of the outer surface layer. The speed of carbon-based micromotors is a compromise between two opposite forces: the increased catalytic activity because of improved fuel decomposition in the inner catalytic layer, which propels their advance, and the friction of the rough outer surface with the fluid, which is opposed to it. The largest outer surface area associated with the highest surface roughness of C60 fullerene and carbon black-Pt micromotors leads to a large friction force, which results in a reduced speed of ∼180 μm/s (1% H_2O_2). In contrast, for carbon-nanotube-Pt based micromotors, the dominant force is the high catalytic activity of the micromotor, which allows them to reach ultrafast speeds up to 440 μm/s (1% H_2O_2). The new protocol opens new avenues for the universal preparation of carbon based multifunctional micromotors for a myriad of practical applications exploiting the features of carbon allotropes.*

INTRODUCTION

Man-made micromotors[1−4] are at the forefront of nanotechnology research due to their great potential in biomedicine,[5,6] environmental remediation,[7−9] energy devices,[10] or in sensing applications.[11,12] Autonomous propulsion of such microscale objects can be achieved by providing an external energy input from a power source (i.e., ultrasound, magnetic, UV light)[13−16] or by means of a chemical reaction occurring at the interface of the device and the liquid environment (i.e., bubble and marangoni-propulsion, self-electrophoresis).[4,17−21] Despite the wide range of potential applications, several challenges should be still faced prior to their practical application, that is, complicated fabrication process, low capacity for cargo transportation, or hampered locomotion in real environments. In this context, artificial micromotors can greatly benefit from the excellent properties of carbon nanomaterials such as thermal conductivities, large surface areas, and biocompatibility to overcome the aforementioned challenges.

Few recent studies indicate that the combination of carbon nanotubes or graphene with metal oxide and metal alloys is a convenient marriage for improving the overall performance in terms of speed and surface chemistry- of artificial micromotors. For example, balloon-like MnO_x−graphene crumbles have been used as "chemical taxis" for micro and nanoactuators.[22] Similarly, Pumera's group developed a graphene micromotor by thermal exfoliation of iridium (Ir)-doped graphite oxide. Oxygen bubbles generated from the decomposition of hydrogen peroxide at the iridium catalytic sites provide highly enhanced propulsion to the micromotor.[23] The incorporation of reduced graphene on SiO_2−Pt based micromotors further demonstrated the key role of such nanomaterial in the enhanced motion and cargo transportation capabilities of the resulting micromotors.[24,25] Graphene coated glass microswimmer, which exhibits directed motions under the influence of electric, magnetic fields, and chemical potential gradients, has also been proposed.[26] Template-prepared microtubular engines offer several advantages over such graphene-based Janus micromotors, that is, low-cost synthesis, easy preparation, improved catalytic performance, and new functionalities for diverse new practical applications.[27] Poly(3,4-ethylenedioxythiophene) micromotors, doped with a mixed Pt nanoparticles (PtNPs)-CNTs-polypyrrol (PPy) catalytic layer, exhibit excellent motion performance in protein-rich media.[28] Graphene-oxide tubular micromotors were shown recently to offer highly efficient propulsion (up to 170 body lengths/s) and operation

at extremely low peroxide levels (0.1%) due to deposition of a microporous Pt inner surface that offered enhanced catalytic activity. Unlike earlier graphene-based micromotors,[29,30] the new microrockets are based on the direct electroreduction of oxide tubular (GO) into the pores of a polycarbonate membrane followed by deposition of a porous inner metal layer.[31] The unique surface properties of graphene allowed for the incorporation of different receptors for ricin detection[32] or the capture and removal of nerve agents and heavy metals.[33,34] Despite these early efforts on the design and application of GO micromotors, the potential of other carbon nanomaterials for advanced nanomachines applications is still a largely unexplored research area.

Here, we will illustrate, for the first time, the template preparation of tubular micromotors using different carbon allotropes, namely 0D (C_{60} fullerene), 1D (carbon nanotubes), 2D (graphene), and 3D (carbon black). Subsequent deposition of diverse inner catalytic layers (Pt, Pd, Ag, Au, or MnO_2) allows for efficient self-propulsion in different complex media. The preparation protocol described here relies on the direct deposition, either electrochemical or directly, of the individual nanomaterial into the pores of a membrane template, leading to functional structures with potential collective properties. Indeed, the new carbon allotropes based micromotors combine the rich outer surface chemistry properties of carbon nanomaterials with the efficient movement of micromotors toward novel future applications such as enhanced pick-up cargo (through the incorporation of specific receptors in the rich outer micromotor surface) and transport (through the enhanced catalytic area) of cargoes. The morphology and outer surface roughness of the resulting micromotors are characterized in the following sections by atomic force microscopy (AFM) and scanning electron microscopy (SEM). Unlike previously reported findings,[24,25] the extremely high surface roughness of 0D- (C_{60} fullerene) and 3D- (carbon black) based micromotors dramatically increases their friction with the liquid media, which results in a great reduction in their speed. Less-rough 1D- and 2D-micromotors exhibit ultrafast bubble propulsion with similar speeds to that observed for graphene-based micromotors.[31] The effect of different inner catalytic layers will be also characterized toward efficient operation in different real media including seawater, serum, and juice samples. The new protocol opens new avenues for the universal preparation of a wide "nanolibrary" of carbon based micromotors for a myriad of practical applications.

EXPERIMENTAL SECTION

Reagents and Equipment. Fullerene-C_{60} (C_{60}, Catalog No. 379646), carboxylic functionalized single-walled carbon nanotubes (SWCNTs-COOH, 0.7−1.3 nm diameter, Catalog. No. 704113), multiwalled carbon nanotubes (MWCNTs, Catalog. No. 659258), and carbon black (CB, < 50 nm particle size, Catalog. No. 699632) were obtained from Sigma-Aldrich (Madrid, Spain) and used without further purification. Partially reduced graphene oxide (rGO) was purchased from GRAPHENEA (Cambridge, MA, USA). Template electrochemical deposition of the micromotors was carried out using an Autolab PGSTAT 12 (Eco Chemie, Utrecht, The Netherlands). SEM images were obtained with a NovaNano FE-SEM 230 FEI instrument using an acceleration voltage of 10 kV. Energy-dispersive X-ray mapping analysis was performed using a Bruker X flash 4010 EDX detector attached to SEM instrument using an acceleration voltage of 22 kV. The AFM experiments were performed with a Nanoscope IIIA equipment (from Veeco) operating under ambient conditions in the dynamic mode. Silicon cantilevers (from Bruker) with a nominal radius of 8 nm and a force constant close to 40 N/m were employed. As the micromotors were scattered over the mica or silicon flat substrates without any specific attachment, a careful measurement strategy had to be followed. First, a given micromotor was chosen, and the cantilever was addressed to land on this structure thanks to the optical microscope attached to the AFM system. Second, because of this lack of attachment between the micromotor and the surface, the tip once centered on the structure has to be swept over the micromotor with the slow x-axis parallel to the longest axis of the micromotor. In the other cases, particularly when the scanning x-axis was orientated across the micromotor (i.e., along the diameter of the micromotor), the micromotor was displaced over the substrate or even became attached to the cantilever tip. The diameter of the micromotors was close to 5 μm, whereas the z-piezo range of the scanner EV (Bruker) used in the measurements was appreciably shorter. Accordingly, to avoid further problems due to this fact, small square areas were scanned, or rectangular areas, with the longest axis along the micromotor longest axis, were chosen to be measured. These images were processed with Gwyddion software to subtract the large curvature of the micromotors to allow discerning their smaller nanometer features and morphology. An inverted optical microscope (Nikon Eclipse Instrument Inc. Ti−S/L100), coupled with 10× and 20× objectives, and a Hamamatsu digital camera C11440 and NIS Elements AR 3.2 software, was used for capturing movies at a rate of 25 frames per second. The speed of the micromotors was tracked using a NIS Elements tracking module. The average micromotor speed was calculated by tracking a total number of 15 micromotors ($n = 15$). Error reported for each value corresponds to the standard deviation of the measurements ($n = 15$). Aqueous hydrogen peroxide solutions, with concentrations ranging from 0.01%−5%, were used as chemical fuel. Sodium cholate was used as surfactant in all water, seawater, and serum propulsion experiments; sodium dodecyl sulfate (Catalog No. 71727, Sigma-Aldrich) was used as surfactant in all juice propulsion experiments.

Electrochemical Synthesis of Carbon Nanomaterial Micromotors. Carbon nanomaterial micromotors were prepared by electrochemical reduction or direct deposition (CB) of the different nanomaterials into the 5 μm-diameter conical pores of a polycarbonate membrane (Catalog No. 7060−2513; Whatman, New Jersey, USA). A thin gold film was first sputtered on the branched side of the membrane to serve as a working electrode. The membrane was then assembled in a Teflon plating cell with aluminum foil serving as an electrical contact for the subsequent electrodeposition. C_{60}, MWCNTs and rGO (0.1 mg mL^{-1}) were first dispersed in a solution containing 0.1 M H_2SO_4 and 0.5 M Na_2SO_4 and sonicated until homogeneous suspension was obtained. SWCNTs-COOH and CB were dispersed in a solution containing 0.5 M Na_2SO_4 by ultrasonication for 15 min. The simultaneous electrochemical reduction and deposition of the carbon nanomaterials were carried out using cyclic voltammetry (CV, over +0.3 to −1.5 V vs Ag/AgCl, 3 M, at 50 mV s^{-1}, for 5, 10, or 20 cycles) using a Pt wire as counter electrode. In addition, CB were also synthesized by a direct procedure; the CB dispersion was dipped into the Teflon cell and allowed to stand for 30 min to promote CB film formation in the pores of the membrane template. Subsequently, a metal tube layer was plated inside the reduced carbon layer. For carbon-Pt, inner Pt layer was galvanostatically deposited at −2 mA for 1000 s from a commercial platinum plating solution (Platinum RTP; Technic Inc., Anaheim, CA).

For carbon-PtNP, the inner PtNPs layer was deposited by amperometry at −0.4 V for 750 s from an aqueous solution containing 4 mM of H_2PtCl_6 in 0.5 M boric acid. For carbon-Ag, the inner Ag layer was deposited at −1.2 V for 6 C from an aqueous solution containing 10 mM $AgNO_3$ in 0.2 M $NaClO_4$ at pH of 3.5 (adjusted with $HClO_4$). For carbon-Pd, inner Pd layer was deposited at −0.65 V for 16 C from an aqueous solution containing 4 mM of $PdCl_2$ in 0.2 M $HClO_4$. For carbon-MnO_2, inner MnO_2 layer was amperometrically deposited at +1.0 V for 1.3 C from aqueous solution of 0.01 M manganese(II) acetate tetra-hydrate. For carbon-Au, inner Au layer was amperometrically deposited at −1.0 V for 1 C from a commercial gold plating solution (Orotemp 24 RTU RACK; Technic Inc.). After

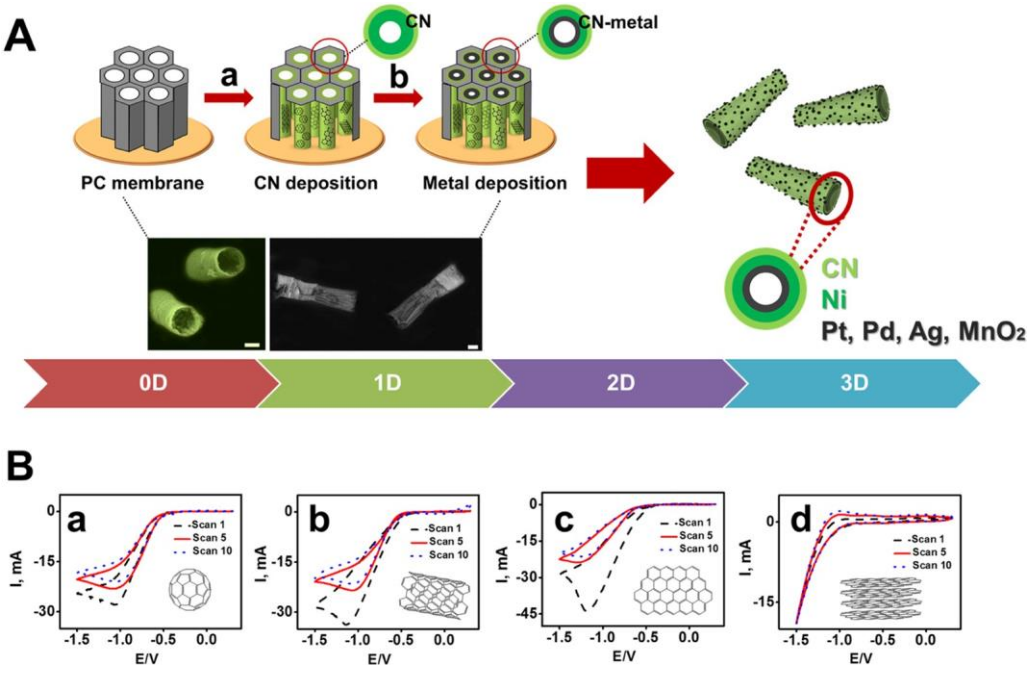

Figure 1. Template electrodeposition of the different carbon allotrope nanomaterials (CN)-metal tubular micromotors. (A) Schematic of the template-based fabrication procedure: (a) electrodeposition of CNs, (b) deposition of Pt, Pd, Ag, Au, or MnO_2 layers. SEM images of MWCNTs-Pt and C_{60}−Pt micromotors. (B) Cyclic voltammograms corresponding to the electrochemical reduction of (a) C_{60} fullerene, (b) MWCNTs, (c) graphene oxide, or (d) carbon black. Scans $n = 1$ (black dash line), $n = 5$ (red solid line), and $n = 10$ (blue dotted line). Scale bars, 1 μm.

metal deposition, the sputtered gold layer was gently removed by hand polishing with 1 μm alumina slurry. The membrane was then dissolved in methylene chloride for 15 min (2 times) to completely release the micromotors. The micromotors were then collected by centrifugation at 7000 rpm for 3 min and washed repeatedly with isopropanol, ethanol, and ultrapure water (18.2 Ω cm), with a 3 min centrifugation following each wash. All micromotors were stored in ultrapure water at room temperature when not in use. The template preparation method resulted in reproducible micromotors.

Catalase Immobilization. The Au inner layer was first modified with an alkanethiol monolayer by overnight incubation in a ethanolic solution containing 7.5 × 10^{-3} M of 6-mercaptohexanol and 2.5 × 10^{-3} M of 11-mercaptoundecanoic acid. Subsequently, the micromotors were rinsed with water for 5 min and transferred to an eppendorf vial containing 200 μL of 4-morpholineethanesulfonic acid (MES) solution (25 × 10^{-3} M, pH 6.5) and the coupling agents, 1-ethyl-3-[3-(dimethylamino)propyl] carbodiimide hydrochloride (0.4 M), *N*-hydroxylsulfosuccinimide (0.1 M), and the catalase enzyme (2 mg mL^{-1}) and incubated for 7 h at 37 °C. This step was followed by two 15 min rinsing steps with PBS-Tween (pH 5.5). Finally, the micromotors were washed three times with water to remove the excess of catalase and then suspended in 5.5 pH buffer and stored at 4 °C. This suspension can be stored for up to 1 week without any change in the micromotor activity.

RESULTS AND DISCUSSION

Figure 1A illustrates the template electrodeposition protocol for the fabrication of carbon nanomaterial-metal bilayer micromotors. As can be seen, C_{60} fullerene (C_{60}), multiwalled carbon nanotubes (MWCNTs), single walled carbon nanotubes (SWCNTs), and reduced graphene oxide (rGO) were deposited on the inner wall of a PC membrane by cyclic voltammetry (CV) followed by plating of a second metallic catalytic/magnetic layer (Pt, Pt−Ni, Pd, Ag, Au, MnO_2). The metallic layer is a critical element for achieving an efficient propulsion as well as for maintaining the shape and mechanical stability of the micromotors. Electrochemical deposition was achieved by cycling the potential between +0.3 and −1.5 V (vs Ag/AgCl, 3 M) at a scan rate of 50 mV s^{-1} for ten cycles. Figure 1B shows the CV corresponding to the reduction ($n = 1$, 5, and 10 scans) of the different materials assayed. The reduction peak decreases while the potential cycling proceeds, which implies a reduction in their structures (except for carbon black). Electrochemical reduction of C_{60} fullerene in aqueous media leads to the formation on an adventitious polyepoxidated $C_{60}O_n$ intermediate with subsequent chemically irreversible loss of "O_2" as water.[35] Such substantial change in the C_{60} structure initiates a "polymer-like" deposition process (reductively initiated polymerization), leading to the formation of a $(-C_{60}O-C_{60}O-)_n$ structure within the walls of the PC membrane.[36,37] In the case of carbon nanotubes and partially reduced GO, as the potential cycling proceeds the initial structure of such nanomaterials is partially modified and the oxygen functionalities are mainly removed. Such reduction in oxygen moieties results in an increase in the number of sp^2 carbons and the hydrophobicity of the resulting carbon nanotubes or graphene films. Under these conditions, MWCNTS, SWCNTs, or graphene layers tend to aggregate between them via π−π interactions and within the walls of the membrane by hydrophobic interactions.[38,39] For CB, no apparent reduction peaks were observed in the CV, although well-defined micromotors (see Figure 1B(d)) were obtained. Because of the hydrophobic nature of the surface of carbon black nanoparticles, they tend to aggregate in solution resulting in nanosized-aggregates, which subsequently interact with the pores of the membrane template. Thus, CB in spheroid form (Ø ≤ 50 nm) does not present highly reactive "oxygen" or other functional groups for enhanced reactivity and solubility. In addition, we use an aqueous phase for CB dispersion; thus, they tend to adhere at "apolar" (not charged) surfaces. Since CB-NPs are not stabilized by a capping agent, their tendency thus to adhere to apolar surfaces is particularly high.[40] The PC

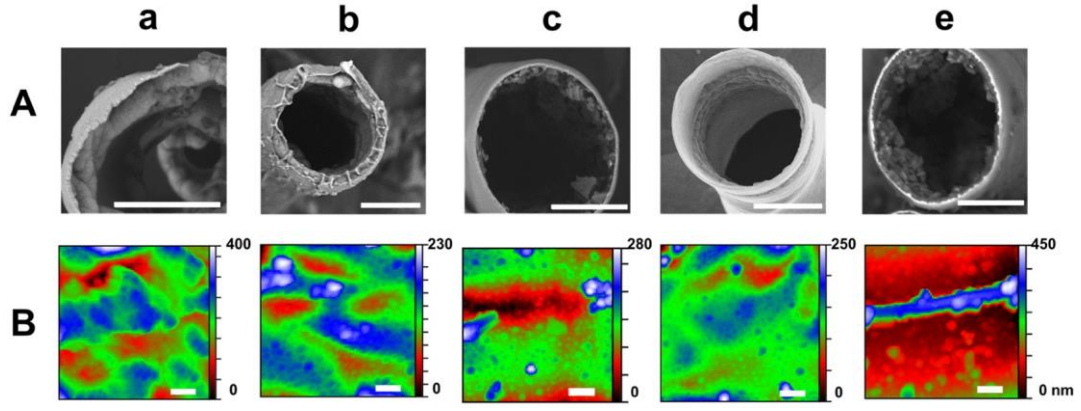

Figure 2. Characterization of the carbon allotrope-metal tubular micromotors. (A) SEM images showing the top-view of the bilayer tube structure and (B) AFM topographical images showing the surface morphology of (a) C_{60}−Pt, (b) SWCNTs-Pt, (c) MWCNTs-Pt, (d) rGO-Pt, and (e) CB-PtNPs micromotors. Scale bars, 1 μm (SEM images) and 200 nm (AFM images). AFM images were processed with Gwyddion software to subtract the large curvature of the micromotors to better display their morphology at the nanometer level.

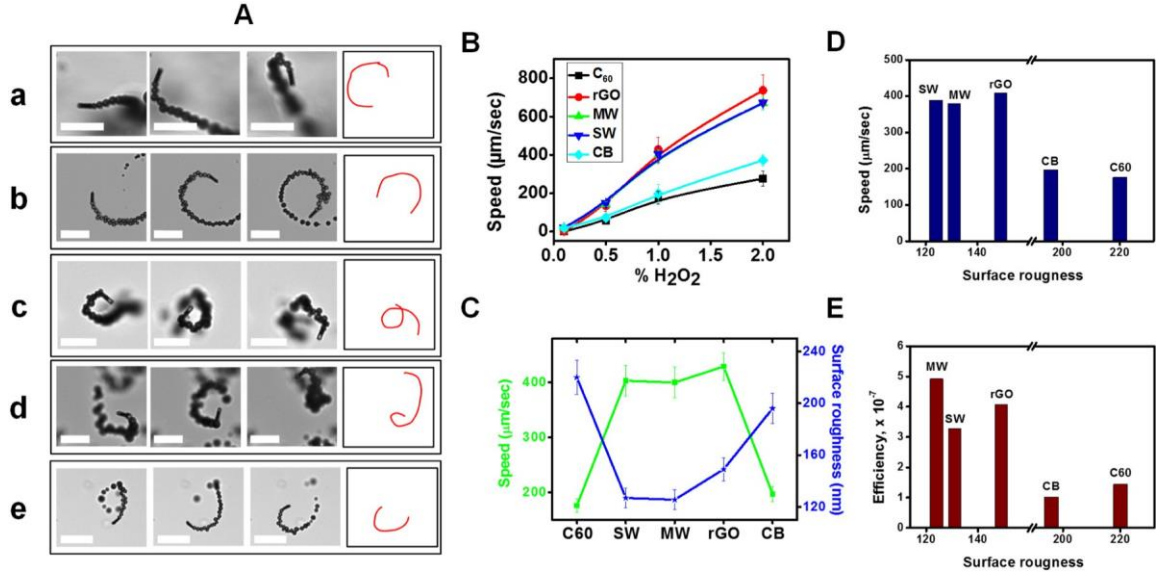

Figure 3. Propulsion of carbon nanomaterial-Pt tubular micromotors. (A) Time-lapse images (250 ms intervals, taken from Supporting Information Videos 1 and 2) and corresponding tracking lines (750 ms period) of the motion of (a) C_{60}−Pt, (b) SWCNTs-Pt, (c) MWCNTs-Pt, (d) rGO-Pt, and (e) CB-Pt micromotors in the presence of 1% H_2O_2. Scale bars, 40 μm. (B) Dependence of the speed of the different micromotors upon the hydrogen peroxide concentration over the 0.1−2% range (n = 15, each data point is the average of 15 measurements). (C, D) Graphics comparing the speed (1% H_2O_2) and surface roughness (as obtained by AFM) of the different carbon-based micromotors. (E) Graphic comparing the efficiency (1% H_2O_2) and surface roughness on the different micromotors. Other conditions: surfactant, 1.5% (w/v) sodium cholate.

membrane triggers then the deposition of the CB-NPs, leading to a continuous carbon film that is subsequently stabilized by the Pt layer. To further verify this hypothesis, we perform a control experiment with CB dispersion without applying any cyclic scans. The as-obtained micromotors have a very well-defined structure, with a thin outer CB layer and an inner Pt layer, as will be described in the following section.

The effect of carbon nanomaterial electrodeposition time was evaluated by varying the number of CV scans from 2 to 20 (except for CB) and using platinum as second metallic layer. Low content of carbon nanomaterial was electrodeposited after 2 scans, which resulted in not well-defined structures that tended to collapse easily. Defined surface morphology and efficient propulsion in peroxide solutions were observed after 5 and 10 cycling scans with no noticeable difference in the structure of the micromotors. However, a high deposition yield, resulting in a high number of micromotors, was obtained after 10 cycling scans. Increasing the number of scans led to the complete coverage of the pore opening, which thus prevented the subsequent deposition of the metallic layer. During the electrodeposition, the carbon nanomaterials nucleate and grow preferentially on the pore walls to reach a defined thickness that can be controlled with the number of cycling scans (i.e., time). As the thickness of microtube wall increases, the order within the nanostructures decreases. Thus, if the polymerization time is too long, a thin film is formed on the top of the microtube, which blocks it completely. Subsequent metal deposition results in the formation of a metallic layer on top of the microtubes, which would prevent their effective movement and efficient propulsion in hydrogen peroxide rich media. This is clearly shown in the SEM image of Figure S2, which shows a rGO-Pt microtube synthesized by using 15 CV scans for graphene deposition. It can be clearly seen the blockage on the top of the microtube and the thin Pt film formed on top. Metal deposition

time was similarly optimized, and the best conditions are listed in the Experimental Section. Figure 2A and B display the SEM and AFM characterization of the resulting micromotors under the optimized conditions. The cross-view SEM images of Figure 1A(a−e) reveal that in all cases, the micromotors have a well-defined structure with a thin outer C_{60}, SWCNTs, MWCNTs, rGO, or CB layer (~50 to 110 nm) and a Pt layer composed of granular particles with average diameters of ~100 nm. Such nanoparticles-based porous metallic structure can be directly related to the presence of higher boundaries and surface roughness of the thin outer carbon layer.

The outer morphology and surface roughness of the resulting carbon nanomaterial-Pt micromotors were then characterized by AFM. Figure 2B displays the topographical images of different micromotors over ~1 μm^2 area. The surface has a granular peak-and-valley type morphology, with the roughness varying greatly depending on the type of carbon nanomaterial, with valleys indicated in red color and protrusions in green to blue color (see Figure 2B, note the different length scales). The average roughness values for C_{60}, SWCNTs, MWCNTs, rGO, and CB were 220 ± 29 nm, 127 ± 10 nm, 126 ± 9 nm, 149 ± 13 nm, and 196 ± 23 nm, respectively (n = 5 micromotors). To further confirm these experimental observations, the normalized outer surface area of the micromotors was also calculated by dividing the surface area of the rockets by the projected area. A similar trend was also observed, as testified in the graphic of Figure S1. Such differences in surface roughness have a strong influence on the propulsion performance of the resulting micromotors, as will be illustrated below.

The time lapse-microscopy images of Figure 3A(a−e) (taken from Supporting Information Videos 1 and 2) illustrate the propulsion of different carbon nanomaterial-Pt micromotors in 1% peroxide solutions. A long tail of oxygen bubbles generated from the catalytic decomposition of H_2O_2 by the rough inner Pt inner layer is released from the rear large-opening side of the micromotors, which propels efficiently as reflected by the moving trajectories depicted in Figure 3A. As can be also seen in Figure 3B, such speed depends on the concentration of peroxide fuel. SWCNTs-Pt, MWCNTs-Pt, and rGO-Pt micromotors reached ultrafast speeds of ~380 ± 60 μm/s (1% H_2O_2), which reflects their larger electrochemical active surface areas and enhanced catalytic properties along with improved fuel accessibility. Such speed is ~2-fold higher than that reported for polyaniline micromotors with similar size but smooth catalytic surface.[41,44] Surprisingly, although the inner Pt layer of C_{60} fullerene and CB micromotors is also composed by a granulate nanoparticulate structure, a greatly diminished speed of 176 ± 25 and 195 ± 29 μm/s was observed in 1% H_2O_2. The efficiency of the micromotors (as energy input conversion into mechanical work) was also calculated following the model described by Mallouk group,[41] and the results obtained are listed in Table S1. The efficiency of C_{60}-Pt, MWCNTs-Pt, SWCNTs-Pt, rGO-Pt, and CB-Pt micromotors in 1% H_2O_2 was found to be 1.44 × 10^{-7}, 3.28 × 10^{-7}, 4.92 × 10^{-7}, 4.08 × 10^{-7}, and 1.02 × 10^{-7}, respectively. This efficiency is higher than previously reported for Ag (5.81 × 10^{-8}, 9% H_2O_2) and MnO_2 micromotors (1.16 × 10^{-8}, 12% H_2O_2) and for Pt-based tubular rolled-up micromotors in 3% H_2O_2 (2.40 × 10^{-10}).[42,43] Note also the influence of the nature of the carbon allotrope upon the efficiency of the different micromotors prepared in this work. Indeed, the graphics of Figure 3C and D compare the speed of the micromotors with their corresponding surface roughness. A defined trend can be clearly observed, with a decrease in the average speeds of the micromotors as the surface roughness increases. Different surface roughness and hence drag forces result in changes of motor speeds of various carbon allotropes. In some cases, such as PtNPs, motor speed is determined by the propulsion forces. Thus, as shown in Table S1 and Figure 3E, different carbon allotropes lead to a change in oxygen evolution rates and, likewise, propulsion forces. Such variation of propulsion forces contributes to the motor speed changes of carbon allotropes as well.

As previously described, the speed of carbon-based micromotors is the result of the balance between two opposite forces: the increased catalytic activity with improved fuel decomposition in the inner catalytic layer and the friction of the rough outer surface with the fluid. Bubble propelled carbon nanomaterial-Pt micromotors movement is based on the decomposition of H_2O_2 fuel into O_2 bubbles and water, catalyzed by platinum. The ejection of such oxygen bubbles through the large end opening of the micromotors pushes the micromotor forward. Thus, two main forces act on the micromotor during its movement: a drag force caused by the fluid and a propulsion force caused by the growth and ejection of bubbles.[43] In fluid dynamics, drag or fluid resistance is a force acting opposite to the relative motion of any object moving with respect to a surrounding fluid. At low Reynolds number, the speed of the micromotor decreased with an increase in the drag force, whereas the propulsion force is assumed to be constant. As recently proposed by Li et al.,[44] the drag force of conical micromotors can be calculated as follows:

$$F = \frac{2\pi\mu L v_{j(t)}}{\ln\left(\frac{L}{b}\right) + c_1} \quad (1)$$

where F is the drag force, μ is the dynamic viscosity of the fluid, L is the length of the micromotor, v_j is the velocity of the micromotors, c_1 is a dimensionless coefficient that depends on the shape and morphology of the micromotor, and b is the cross-sectional radius of the micromotor in the middle.[45] Such drag force, F, during movement is primarily ascribed to the outer surface of the micromotors rather than to the inner catalytic surface. In this context, the above-mentioned dimensionless coefficient c_1 is related with the drag coefficient C_d by the drag equation coefficient, as follows:[45]

$$C_d = \frac{4\xi^2}{R_e} \Big/ \left(\ln\frac{2\xi}{2 - \xi\tan\theta} + c_1\right) \quad (2)$$

where $\xi = L/R_{max}$, θ is the semicone angle, and R_e is the Reynolds number. According to eq 2, the drag coefficient C_d is not only determined by R_e, but also by the geometry and outer surface parameters of the micromotors. The friction force represented by the drag coefficient is proportional to the contact area between the micromotor and the fluid. The largest outer surface area associated with the largest surface roughness of C_{60} and CB-Pt micromotors leads to the largest friction force among the different carbon micromotors evaluated, which results in the largest drag coefficients C_d. According to eq 2, as the drag coefficient C_d increases, the dimensionless coefficient c_1 decreases. Such coefficient c_1 is also inversely proportional to the drag force value F, as shows in eq 1. The increase in the drag coefficient-associated with the increased friction with the fluid results in a drastic increase in the drag force, F, which leads to the drastic observed reduction in the speed of C_{60} and CB-Pt

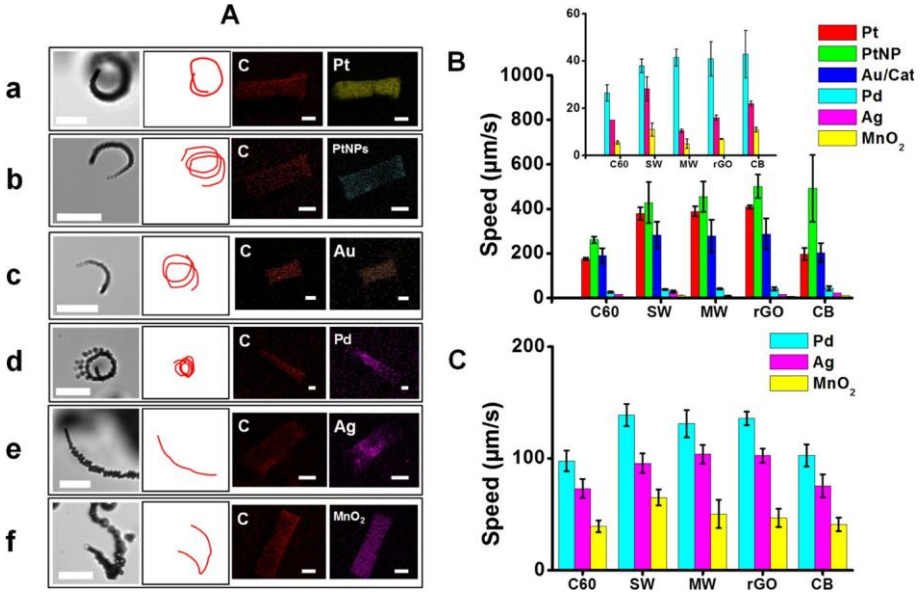

Figure 4. Preparation and propulsion performance of carbon nanomaterial with several catalytic metals. (A) Time-lapse images (taken from Supporting Information Videos 3 and 4) and corresponding tracking lines (500−1000 ms period) of the motion of (a) CB−Pt, (b) SWCNTs-PtNPs, (c) rGO-Au-catalase, (d) MWCNTs-Pd, (e) SWCNTs-Ag, and (f) C_{60}-MnO_2 micromotors in the presence of (a, b, c) 1% or (d, e, f) 5% H_2O_2. Scale bars, 40 μm. Right part shows EDX images illustrating the distribution of carbon and the specific metal in the micromotors. Scale bars, 5 μm. (B, C) Speed profiles of the different carbon−metal based micromotors at 1% or 5% H_2O_2, respectively (n = 15, each data point is the average of 15 measurements). Top inset of panel B shows the speed of Pd, Ag, or MnO_2 carbon allotrope micromotors. Other conditions: surfactant, 1.5% (w/v) sodium cholate.

micromotors. In the latter case, the dominant force is the friction with the fluid, whereas for MWCNTs, SWCNTs, and rGO micromotors, it is the high catalytic activity of the micromotor. This behavior might have strong implications for future practical applications of the developed micromotors.

We next evaluated the effect of the inner morphology of the different carbon nanomaterials for the deposition of different catalytic inner metallic layers, including platinum nanoparticles (PtNPs), palladium, silver, manganese dioxide, and gold for biocatalytic propulsion. As can be seen in the EDX mappings of Figure 4A, the high conductivity of the carbon-based layer favors the deposition of the different metals, which are well-distributed along the micromotors. Figure 4A illustrates the efficient propulsion of CB-Pt, SWCNTs-PtNPs, and rGO-Au-catalase, which propel at speeds of 197 ± 27, 430 ± 91, and 321 ± 35 μm/s, respectively, in 1% H_2O_2 (see also Supporting Information Videos 3 and 4). The remarkably high speed of the PtNPs and Au-catalase based micromotors reflects the increase in the inner catalytic surface area for improved fuel decomposition.[31] Such trend is also observed using other carbon-based micromotors as supporting layers for PtNPs and Au (see Figure 4B). As can be clearly seen from the SEM images of Figure 2, a rough catalytic Pt patch is observed for the different carbon allotropes-Pt micromotors. A higher roughness can be clearly observed in the case when Pt was deposited in the form of nanoparticles (Figure 2A(e)), which results in improved fuel accessibility but most importantly in much higher surface area for H_2O_2 decomposition. Similar results were observed in all cases with the different carbon nanomaterials. Indeed, clear structure differences can be observed when comparing Pt and PtNPs inner layers. Thus, as shown in the SEM images of Figure S3, when Pt is galvanostatically deposited, a rough Pt layer, composed by peak and valleys of granular nanoparticles, can be observed (left image). On the other hand, when Pt is deposited in the form of nanoparticles a distinct morphology, composed by well-defined granular individual nanoparticles, can be observed. The micromotors based on PtNPs are much less affected by the roughness of the outer carbon layer. To fully reveal the critical role of carbon allotropes to improve the average micromotor speed and performance, we performed a series of experiments using smooth poly(3,4-ethylenedioxythiophene) (PEDOT) micromotors as support for the PtNPs. The control PEDOT-PtNPs micromotors move at speed of over 89 μm/s (1% H_2O_2), which is up to ∼5-times slower than those observed for carbon nanomaterials-PtNPs based micromotors, which reached speeds of ∼300−500 μm/s (1% H_2O_2) (see also Supporting Information Video 5). Higher SEM magnification images (see Figure S4) illustrate that the inner Pt layers of PEDOT micromotors display a smooth surface, as compared with the very rough morphology of carbon-based nanomaterials micromotors. This further reveals that under the experimental conditions employed here, the PEDOT film is not an adequate support for the nucleation of PtNPs. The unique structure of carbon nanomaterial based micromotors can be attributed to the presence of a high density of intragrain and grain-boundary defects in the carbon-nanomaterials based layer, revealing thus the critical role of the rich chemistry of carbon allotropes in comparison with common polymers such as PEDOT. The intermittent layers of carbon allotropes that form the shell of the microengine imply the presence of large number of edges and defects in such thin carbon films. Pt layers thus tend to nucleate and grow from the defects of carbon sheets, leading to such porous structures. It is also well-known that carbon atoms with dangling bonds or oxygen functional groups (such as that one existing in our carbon allotropes layer) enhance the interaction between the inner carbon structure and Pt clusters, stabilizing the porous structure and improving its catalytic properties. Figure 4A displays also the time lapse images (taken from Supporting Information Video 5) and corresponding

tracking lines of MWCNTs-Pd, SWCNTs-Ag, and C_{60} fullerene-MnO_2 micromotors, which require a five-fold increase in peroxide levels (5%) to move at average speeds of 131 ± 12, 96 ± 9, and 39 ± 5 μm/s, respectively. Similar results were obtained using different carbon nanomaterials inner layers (see Figure 4C and Table S2). Such decrease in the speed can be attributed to the lower catalytic activity of such metals toward hydrogen peroxide decomposition. With regard to Pd, to our knowledge, this is the first time that is used as catalytic metal for tubular micromotors. Early attempts to use smooth polymeric tubes as supporting material indicated that Pd tends to deposit at the top of the tube and block the microtubule for fuel accessibility.[46] The high conductivity of our carbon-based layer favors the deposition of palladium as illustrated in the images of Figure 4A(d). The speed of Ag based micromotors is similar to that reported by Wang et al.,[46] for PPy-Ag micromotors (100 μm/s in 5% H_2O_2), but in our case due to the higher loading of Ag catalyst (due to the porous inner structure), the motor displays efficient lifetime of over 1 h as compared with the 40 min described for PPy smooth tubes. Higher speeds have been reported by Pumerasteam for concentric Cu−Ag micromotors (254 μm/s, 3% H_2O_2),[47] mainly due to the much higher loading of exposed silver that covers completely half part of the micromotors. Pumera also reported the first example of H_2O_2 driven MnO_2 micromotor, which propels at a speed of ∼50 μm/s in 12% fuel levels.[43] Also, and unlike our carbon based micromotors, similar sized PEDOT-MnO_2 or MnO_2 tubular micromotors[48] do not exhibit efficient propulsion at peroxide levels below 5% H_2O_2.

The efficient propulsion of the different carbon nanomaterial-metal tubular micromotors was also evaluated in complex media toward future practical applications. The time-lapse images of Figure 5A, taken from Supporting Information Video 6, illustrate the efficient propulsion performance of CB-Pt micromotors in salt-rich media, that is, seawater, C_{60}-Pt micromotors in raw human serum, and MWCNTs-Pt micromotors in juice samples. Similar studies were made with rockets prepared with the different carbon-supporting layers and catalysts, Pt and PtNP, at 1% levels. Despite the viscosity and complexity of the media, the motors still operate at considerable speed between ∼19 and 174 μm/s depending on the sample and micromotor employed. Figure 5B,C and Table S1 show the speed profiles of the different carbon−metal based micromotors in seawater, juice, and human serum using different catalysts. The lowest speeds in all cases were observed in juice samples, followed by seawater and human serum. Also, the highest speeds were reached with PtNPs and Pt-based micromotors and the lowest ones with Ag, Pd, and MnO_2 micromotors. The different speeds in the different media assayed reflect the different viscosity and complexity of the media employed. It is well-known that the speed of these micromotors is salt independent.[49,50] Thus, the observed trend can be explained by two different factors, that is, the low speed noted in the different media assayed reflects the increased viscosity in the media (1 cP in water as compared with 1.5 cP and 1.2 cP in plasma and seawater, respectively).

A second explanation can be attributed to the increased complexity of the samples tested. For instance, serum and juice contain dissolved proteins, carbohydrates, and electrolytes that can adsorb in the catalytic surface, hindering thus the micromotor motion.[51] From this library, the selection of each micromotor will depend on the specific application and sample. For example, PtNPs based micromotors are suitable for further

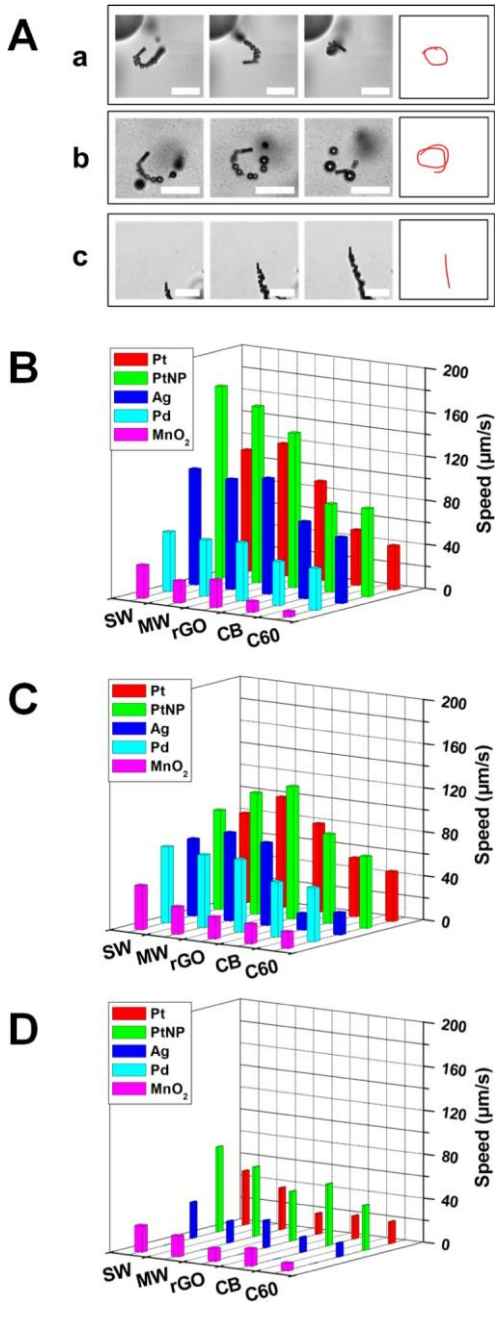

Figure 5. Efficient propulsion of carbon nanomaterial-metal tubular micromotors in complex media. (A) Time-lapse images (taken from Supporting Information Video 6) and corresponding tracking lines (1000 ms period) of the motion of (a) CB−Pt micromotors in seawater, (b) C_{60}-Pt micromotors in human serum, and (c) MWCNTs-Pt micromotors in juice samples. Scale bar, 40 μm. (B, C, D) Speed profiles of the different carbon−metal based micromotors in seawater, human serum, and juice, respectively (n = 15, each data point is the average of 15 measurements). Other conditions: 1% (for Pt and PtNPs-based micromotors) or 5% (for Ag, Pd and MnO_2 micromotors) H_2O_2, surfactant, 1.5% (w/v) sodium cholate.

functionalization and cargo transportation. Also, a magnetic layer (Ni) can be easily incorporated in the micromotor structure for efficient magnetic control/guidance of the micromotor, as shown in the microscopy images of Figure S4 and Supporting Information Video 7. The low cost of Ag and MnO_2, the generation of reaction products and radicals during their reaction with H_2O_2,[51] along with their rich outer

chemistry (imparted by the carbon nanomaterial), make these micromotors particularly attractive for specific applications, that is, decontamination.[52]

CONCLUSIONS

We have described the synthesis and characterization of C_{60} fullerene, SWCNTs, MWCNT, rGO, and carbon black based micromotors. The micromotors are easily and inexpensively prepared by direct electrochemical reduction of the nanomaterial into the pores of a membrane template. Diverse inner catalytic layers (Pt, Pd, Ag, Au, or MnO_2) have been evaluated for efficient bubble motor propulsion in different media. AFM and SEM characterization reveals that the speed of carbon-based micromotors is the result of the balance between different morphological properties of the micromotors namely, the outer surface roughness, and the inner wall micromotor structure. Thus, the higher the former, the larger the friction force between the moving micromotor and the surrounding fluid, which hampers the micromotor advance. In contrast, depending on the morphology of the inner wall of the micromotor, both the reactant accessibility and the surface catalytic area can be largely improved in such way that a dramatic acceleration of the fuel catalytic reaction can be achieved and thus the micromotor movement be enhanced. The largest outer surface area associated with the largest surface roughness of C_{60} fullerene and carbon black-Pt micromotors leads to a large friction force, which results in ~2.7-fold decrease in the speed as compared with carbon-nanotube-Pt based micromotors. The new protocol opens new avenues for the universal preparation of a wide "nanolibrary" of carbon based multifunctional micromotors for a myriad of practical applications. While peroxide-driven motors are used for proof-of-concept here, other practical uses can be achieved by the replacement of the Pt catalyst by a Mg or Zn catalytic layer for water driven propulsion. Alternatively, the new micromotor concept can be applied using fuel-free ultrasound, magnetic propelled, or electric field propelled micromotors.[53] Indeed, current efforts are aimed at our lab to demonstrate the unique functionality of carbon allotropes-Pt micromotors for the enhanced cargo pick-up and transport in lab-on-a-chip devices and for on−off detection of clinically relevant analytes. It is time for opening and exploring real application involving not only health care and environmental remediation, but also in the food safety sector by exploring the newly developed nanomaterial-based micromotors.

ASSOCIATED CONTENT

Supporting Information

The Supporting Information is available free of charge on the ACS Publications website at DOI: 10.1021/acs.chemmater.6b03689.

Additional experimental details and figures (PDF)
Propulsion of C_{60} fullerene-Pt, SWCNTs-Pt, and MWCNTs-Pt micromotors in 1% H_2O_2 (AVI)
Propulsion of CB-Pt and rGO-Pt micromotors in 1% H_2O_2 (AVI)
Propulsion of CB-Pt, SWCNTs-PtNPs, and rGO-Au-catalase micromotors in 1% H_2O_2 (AVI)
Propulsion of MWCNTs-Pd, SWCNTs-Ag, and C_{60} fullerene MnO_2 micromotors in 5% H_2O_2 (AVI)
Propulsion of PEDOT-PtNPs and SWCNTs-PtNPs in 1% H_2O_2 (AVI)
Efficient propulsion of CB-Pt, C_{60}fullerene-Pt, and MWCNTs-Pt micromotors in seawater, human serum, and juice samples (AVI)
Efficient magnetic guidance of MWCNTs-Ni-PtNPs micromotors (AVI)

AUTHOR INFORMATION

Corresponding Authors

*E-mail: beatriz.jurado@uah.es.
*E-mail: alberto.escarpa@uah.es.

ORCID

A. Escarpa: 0000-0002-7302-0948

Author Contributions

The manuscript was written through contributions of all authors. All authors have given approval to the final version of the manuscript.

Notes

The authors declare no competing financial interest.

ACKNOWLEDGMENTS

B.J.-S. acknowledges support from the People Programme (Marie Curie Actions) of the EU seventh Framework Programme (FP7 2007−2013) under REA Grant No. PIOF-GA-2012−326476 and from the Ministry of Economy and Competitiveness (Ramon y Cajal contract, RYC-2015−17558). R.M.-H. acknowledges the FPI fellowship received from the Ministry of Economy and Competitiveness (BES-2015−072346). A.E. acknowledges financial support from the Spanish Ministry of Economy and Competitiveness (CTQ2014−58643-R) and the NANOAVANSENS program (S2013/MIT-3029) from the Community of Madrid. We thank A. Valera (ICMM-CSIC) for the SEM measurements.

REFERENCES

(1) Paxton, W. F.; Kistler, K. C.; Olmeda, C. C.; Sen, A.; St Angelo, S. K.; Cao, Y.; Mallouk, T. E.; Lammert, P. E.; Crespi, V. H. Catalytic Nanomotors: Autonomous Movement Of Striped Nanorods. *J. Am. Chem. Soc.* 2004, *126*, 13424−13431.

(2) Ozin, G. A.; Manners, I.; Fournier-Bidoz, S.; Arsenault, A. Dream Nanomachines. *Adv. Mater.* 2005, *17*, 3011−3018.

(3) Mei, Y.; Solovev, A. A.; Sanchez, S.; Schmidt, O. G. Rolled-Up Nanotech On Polymers: From Basic Perception To Self-Propelled Catalytic Microengines. *Chem. Soc. Rev.* 2011, *40*, 2109−2119.

(4) Wang, J. *Nanomachines: Fundamentals And Applications*; Wiley-VCH, 2013.

(5) Gao, W.; Wang, J. Synthetic Micro/Nanomotors In Drug Delivery. *Nanoscale* 2014, *6*, 10486−10494.

(6) Srivastava, S. K.; Medina-Sanchez, M.; Koch, B.; Schmidt, O. G. Medibots: Dual-Action Biogenic Microdaggers For Single-Cell Surgery And Drug Release. *Adv. Mater.* 2016, *28*, 832−837.

(7) Soler, L.; Magdanz, V.; Fomin, V. M.; Sanchez, S.; Schmidt, O. G. Self-Propelled Micromotors For Cleaning Polluted Water. *ACS Nano* 2013, *7*, 9611−9620.

(8) Uygun, M.; Singh, V. V.; Kaufmann, K.; Uygun, D. A.; de Oliveira, S. D.; Wang, J. Micromotor-Based Biomimetic Carbon Dioxide Sequestration: Towards Mobile Microscrubbers. *Angew. Chem., Int. Ed.* 2015, *54*, 12900−12904.

(9) Teo, W. Z.; Zboril, R.; Medrik, I.; Pumera, M. Fe(0) Nanomotors In Ton Quantities (10(20) units) For Environmental Remediation. *Chem. - Eur. J.* 2016, *22*, 4789−4793.

(10) Singh, V. V.; Soto, F.; Kaufmann, K.; Wang, J. Micromotor-Based Energy Generation. *Angew. Chem., Int. Ed.* 2015, *54*, 6896−6899.

(11) Jurado-Sánchez, B.; Escarpa, A. Milli, Micro And Nanomotors: Novel Analytical Tools For Real-World Applications. *TrAC, Trends Anal. Chem.* 2016, *84*, 48−59.
(12) Duan, W.; Wang, W.; Das, S.; Yadav, V.; Mallouk, T. E.; Sen, A. Synthetic Nano- And Micromachines In Analytical Chemistry: Sensing, Migration, Capture, Delivery, And Separation. *Annu. Rev. Anal. Chem.* 2015, *8*, 311−333.
(13) Wang, W.; Li, S.; Mair, L.; Ahmed, S.; Huang, T. J.; Mallouk, T. E. Acoustic Propulsion Of Nanorod Motors Inside Living Cells. *Angew. Chem., Int. Ed.* 2014, *53*, 3201−3204.
(14) Li, J.; Li, T.; Xu, T.; Kiristi, M.; Liu, W.; Wu, Z.; Wang, J. Magneto-Acoustic Hybrid Nanomotor. *Nano Lett.* 2015, *15*, 4814−4821.
(15) Xuan, M.; Wu, Z.; Shao, J.; Dai, L.; Si, T.; He, Q. Near Infrared Light-Powered Janus Mesoporous Silica Nanoparticle Motors. *J. Am. Chem. Soc.* 2016, *138*, 6492−6497.
(16) Kim, K.; Guo, J.; Liang, Z. X.; Zhu, F. Q.; Fan, D. L. Man-Made Rotary Nanomotors: A Review Of Recent Developments. *Nanoscale* 2016, *8*, 10471−10490.
(17) Wilson, D. A.; Nolte, R. J. M.; Van Hest, J. C. M. Autonomous Movement Of Platinum-Loaded Stomatocytes. *Nat. Chem.* 2012, *4*, 268−274.
(18) Sanchez, S.; Soler, L.; Katuri, J. Chemically Powered Micro- And Nanomotors. *Angew. Chem., Int. Ed.* 2015, *54*, 1414−1444.
(19) Guix, M.; Meyer, A. K.; Koch, B.; Schmidt, O. G. Carbonate-Based Janus Micromotors Moving In Ultra-light Acidic Environment Generated By HeLa Cells In Situ. *Sci. Rep.* 2016, *6*, 21701.
(20) Wang, H.; Moo, J. G.; Pumera, M. From Nanomotors to Micromotors: The Influence Of The Size Of An Autonomous Bubble-propelled Device Upon Its Motion. *ACS Nano* 2016, *10*, 5041−5050.
(21) Zhao, G.; Pumera, M. Liquid−Liquid Interface Motion Of a Capsule Motor Powered By The Interlayer Marangoni Effect. *J. Phys. Chem. B* 2012, *116*, 10960−10963.
(22) Chen, X.; Wu, G.; Lan, T.; Chen, W. Autonomous Micromotor Based On Catalytically Pneumatic Behavior Of Balloon-Like MnO_x-Graphene Crumples. *Chem. Commun.* 2014, *50*, 7157−7159.
(23) Wang, H.; Sofer, Z.; Sheng Eng, A. Y.; Pumera, M. Iridium-Catalyst-Based Autonomous Bubble-Propelled Graphene Micromotors With Ultralow Catalyst Loading. *Chem. - Eur. J.* 2014, *20*, 14946−14950.
(24) Orozco, J.; Mercante, L. A.; Pol, R.; Merkoci, A. Graphene-Based Janus Micromotors For The Dynamic Removal of Pollutants. *J. Mater. Chem. A* 2016, *4*, 3371−3378.
(25) Ma, X.; Katuri, J.; Zeng, Y.; Zhao, Y.; Sanchez, S. Surface Conductive Graphene-Wrapped Micromotors Exhibiting Enhanced Motion. *Small* 2015, *11*, 5023−5027.
(26) Kumar, S.; Singh, A. K.; Dasmahapatra, A. K.; Mandal, T. K.; Bandyopadhyay, D. Graphene Based Multifunctional Superbots. *Carbon* 2015, *89*, 31−40.
(27) Wang, H.; Pumera, M. Fabrication of Micro/Nanoscale Motors. *Chem. Rev.* 2015, *115*, 8704−8735.
(28) Li, Y.; Wu, J.; Xie, Y.; Ju, H. An Efficient Polymeric Micromotor Doped With Pt Nanoparticle@Carbon Nanotubes for Complex Bio-Media. *Chem. Commun.* 2015, *51*, 6325−6328.
(29) Hu, C.; Zhao, Y.; Cheng, H.; Wang, Y.; Dong, Z.; Jiang, C.; Zhai, X.; Jiang, L.; Qu, L. Graphene Microtubings: Controlled Fabrication and Site-Specific Functionalization. *Nano Lett.* 2012, *12*, 5879−5884.
(30) Yao, K.; Manjare, M.; Barrett, C. A.; Yang, B.; Salguero, T. T.; Zhao, Y. Nanostructured Scrolls From Graphene Oxide For Microjet Engines. *J. Phys. Chem. Lett.* 2012, *3*, 2204−2208.
(31) Martin, A.; Jurado-Sanchez, B.; Escarpa, A.; Wang, J. Template Electrosynthesis of High-Performance Graphene Microengines. *Small* 2015, *11*, 3568−3574.
(32) Esteban-Fernández de Ávila, B.; Lopez-Ramirez, M. A.; Báez, D. F.; Jodra, A.; Singh, V. V.; Kaufmann, K.; Wang, J. Aptamer-Modified Graphene-Based Catalytic Micromotors: Off−On Fluorescent Detection of Ricin. *ACS Sensors* 2016, *1*, 217−221.
(33) Vilela, D.; Parmar, J.; Zeng, Y.; Zhao, Y.; Sanchez, S. Graphene-Based Microbots for Toxic Heavy Metal Removal And Recovery From Water. *Nano Lett.* 2016, *16*, 2860−2866.
(34) Singh, V. V.; Martin, A.; Kaufmann, K.; de Oliveira, S. D. S.; Wang, J. Zirconia/Graphene Oxide Hybrid Micromotors For Selective Capture of Nerve Agents. *Chem. Mater.* 2015, *27*, 8162−8169.
(35) Xiao, L.; Wildgoose, G. G.; Crossley, A.; Compton, R. G. The Electroreduction Of "C_{60}" Films in Aqueous Electrolyte Does Not Lead To Alkali Metal Ion Insertion□ Evidence For The Involvement Of Adventitious Poly-Epoxidated C_{60} ($C_{60}O_n$). *Sens. Actuators, B* 2009, *138*, 397−401.
(36) Winkler, K.; Costa, D. A.; Balch, A. L.; Fawcett, W. R. A Study of Fullerene Epoxide Electroreduction And Electropolymerization Processes. *J. Phys. Chem.* 1995, *99*, 17431−17436.
(37) Winkler, K.; Costa, D. A.; Fawcett, W. R.; Balch, A. L. Alteration Of The Electrochemistry Of Fullerene C60 In The Presence Of Dioxygen: Formation Of A Redox-Active Polymeric Film. *Adv. Mater.* 1997, *9*, 153−156.
(38) Wu, K.; Hu, S. Deposition Of A Thin Film Of Carbon Nanotubes Onto A Glassy Carbon Electrode By Electropolymerization. *Carbon* 2004, *42*, 3237−3242.
(39) Martín, A.; Hernández-Ferrer, J.; Vázquez, L.; Martínez, M. T.; Escarpa, A. Controlled Chemistry Of Tailored Graphene Nanoribbons For Electrochemistry: A Rational Approach To Optimizing Molecule Detection. *RSC Adv.* 2014, *4*, 132−139.
(40) Svegl, I. G.; Bele, M.; Ogorevc, B. Carbon Black Nanoparticles Film Electrode Prepared By Using Substrate-Induced Deposition Approach. *Anal. Chim. Acta* 2008, *628*, 173−180.
(41) Wang, W.; Chiang, T. Y.; Velegol, D.; Mallouk, T. E. Understanding The Efficiency Of Autonomous Nano- And Microscale Motors. *J. Am. Chem. Soc.* 2013, *135*, 10557−10565.
(42) Li, J.; Huang, G.; Ye, M.; Li, M.; Liu, R.; Mei, Y. Dynamics Of Catalytic Tubular Microjet Engines: Dependence on Geometry and Chemical Environment. *Nanoscale* 2011, *3*, 5083−5089.
(43) Wang, H.; Zhao, G.; Pumera, M. Beyond platinum: Bubble-Propelled Micromotors Based On Ag and MnO_2 Catalysts. *J. Am. Chem. Soc.* 2014, *136*, 2719−2722.
(44) Li, L.; Wang, J.; Li, T.; Song, W.; Zhang, G. A Unified Model Of Drag Force For Bubble-Propelled Catalytic Micro/Nanomotors With Different Geometries In Low Reynolds Number Flows. *J. Appl. Phys.* 2015, *117*, 104308.
(45) Li, L.; Wang, J.; Li, T.; Song, W.; Zhang, G. Hydrodynamics And Propulsion Mechanism Of Self-Propelled Catalytic Micromotors: Model And Experiment. *Soft Matter* 2014, *10*, 7511−7518.
(46) Gao, W.; Sattayasamitsathit, S.; Uygun, A.; Pei, A.; Ponedal, A.; Wang, J. Polymer-Based Tubular Microbots: Role Of Composition And Preparation. *Nanoscale* 2012, *4*, 2447−2453.
(47) Teo, W. Z.; Wang, H.; Pumera, M. Beyond Platinum: Silver-Catalyst Based Bubble-Propelled Tubular Micromotors. *Chem. Commun.* 2016, *52*, 4333−4336.
(48) Safdar, M.; Wani, O. M.; Jänis, J. Manganese Oxide-Based Chemically Powered Micromotors. *ACS Appl. Mater. Interfaces* 2015, *7*, 25580−25585.
(49) Manesh, K. K.; Cardona, M.; Yuan, R.; Clark, M.; Kagan, D.; Balasubramanian, S.; Wang, J. Template-Assisted Fabrication Of Salt Independent Catalytic Tubular Microengines. *ACS Nano* 2010, *4*, 1799−1804.
(50) Gao, W.; Sattayasamitsathit, S.; Orozco, J.; Wang, J. Efficient Bubble Propulsion Of Polymer-Based Microengines In Real-Life Environments. *Nanoscale* 2013, *5*, 8909−8914.
(51) Wani, O. M.; Safdar, M.; Kinnunen, N.; Jänis, J. Dual Effect Of Manganese Oxide Micromotors: Catalytic Degradation And Adsorptive Bubble Separation Of Organic Pollutants. *Chem. - Eur. J.* 2016, *22*, 1244−1247.
(52) Dey, K. K.; Wong, F.; Altemose, A.; Sen, A. Catalytic Motors□ Quo Vadimus? *Curr. Opin. Colloid Interface Sci.* 2016, *21*, 4−13.
(53) Bouffier, L.; Ravaine, V.; Sojic, N.; Kuhn, A. Electric Fields For Generating Unconventional Motion Of Small Objects. *Curr. Opin. Colloid Interface Sci.* 2016, *21*, 57−64.